

1 **Impact of aerosol hygroscopic growth on retrieving aerosol extinction coefficient** 2 **profiles from elastic-backscatter lidar signals**

3 Gang Zhao¹, Chunsheng Zhao¹, Ye Kuang¹, Jiangchuan Tao¹, Wangshu Tan¹, Yuxuan Bian², Jing Li¹,
4 Chengcai Li¹

5 1 Department of Atmospheric and Oceanic Sciences, School of Physics, Peking University, Beijing,
6 China

7 2 State Key Laboratory of Severe Weather, Chinese Academy of Meteorological Sciences, Beijing,
8 100081, China

9 *Correspondence to: Chunsheng Zhao (zcs@pku.edu.cn)*

10 **Abstract**

11 Light detection and ranging (lidar) measurements have been widely used to profile ambient
12 aerosol extinction coefficient (σ_{ext}). Particle extinction-to-backscatter ratio (lidar ratio, LR), which
13 highly depends on aerosol dry particle number size distribution (PNSD) and aerosol hygroscopicity, is
14 introduced to retrieve the σ_{ext} profile from elastic-backscatter lidar signals. Conventionally, a constant
15 column integrated LR that is estimated from aerosol optical depth is used by the retrieving algorithms.
16 In this paper, the influences of aerosol PNSD, aerosol hygroscopic growth and relative humidity (RH)
17 profiles on the variation of LR are investigated based on the datasets from field measurements in the
18 North China Plain (NCP). Results show that LR has an enhancement factor of 2.2 when RH reaches
19 92%. Simulation results indicate that both the magnitude and vertical structures of the σ_{ext} profiles by
20 using column-related LR method are significantly biased from the original σ_{ext} profile. The relative
21 bias, which is mainly influenced by RH and PNSD, can reach up to 40% when RH at the top of the
22 mixed layer is above 90%. A new algorithm for retrieving σ_{ext} profiles and a new scheme of LR
23 enhancement factor by RH in the NCP are proposed in this study. The relative bias between the σ_{ext}
24 profile retrieved with this new algorithm and the ideal true value is reduced to below 13%.

25 **1. Introduction**

26 Atmospheric aerosols can directly scatter and absorb solar radiation, thus exerting significant
27 impacts on the atmospheric environment and climate change. Vertical distributions of aerosol particles
28 are crucial for studying the roles of atmospheric aerosols in the radiation balance of the
29 Earth-Atmosphere system (Kuang et al., 2016), air pollution transportation (Gasteiger et al., 2017) and

30 boundary layer process. However, there remain many problems while determining the spatial and
31 temporal distributions of aerosols because of their highly variable properties (Anderson and Anderson,
32 2003; Andreae and Crutzen, 1997) and complex sources. As a result, our knowledge about the vertical
33 distributions of aerosols is still very limited.

34 Light detection and ranging (lidar) instruments are useful remote sensing tools to monitor profiles
35 of aerosol optical properties. This kind of instrument involves a pulsed laser beam, which can be used
36 to detect the back-scatter signals from aerosols and air molecules in the atmosphere (Klett, 1981).
37 Elastic-backscatter lidar is one of the most frequently used instruments (He et al., 2006; Pietruczuk and
38 Podgórski, 2009). However, there are some limitations when deriving aerosol extinction coefficient
39 (σ_{ext}) and aerosol back scattering coefficient (β_{sca}) from elastic-backscatter lidar signals. Many efforts
40 have been carried out to retrieve the σ_{ext} profiles from lidar signals (Klett, 1981, 1985). Particle
41 extinction-to-backscatter ratio, which is usually termed as the lidar ratio (LR), is required when
42 retrieving σ_{ext} profiles (Fernald, 1984; Fernald et al., 1972). LR can be derived directly using Raman
43 lidar (Pappalardo et al., 2004b) and high spectral resolution lidar (She et al., 1992; Shipley et al., 1983;
44 Sroga et al., 1983) measurements. Raman lidar has low signal to noise ratios (SNR) during the day,
45 which may lead to significant bias and uncertainties in retrieving lidar signals. High spectral resolution
46 lidar have high technique requirement and expensive first cost. (Ansmann et al., 2002) demonstrated
47 that the profile of LR could be retrieved from Raman lidar and this LR profile can be used to retrieve
48 σ_{ext} profiles from high SNR elastic-backscattering lidar data. However, there exist many cases when
49 elastic-backscatter lidar is used without concurrently measured LR profile.

50 Sun-photometer, radiometer and elastic-backscatter lidar data are usually used simultaneously to
51 retrieve σ_{ext} profiles (Chaikovsky et al., 2016; He et al., 2006). In these studies, σ_{ext} profiles could be
52 retrieved from elastic-backscatter lidar signals by using a constant column-related LR, which is
53 constrained by measurements of aerosol optical depth (AOD) from sun-photometer. However, many
54 factors such as aerosol particle number size distribution (PNSD), aerosol refractive index, aerosol
55 hygroscopicity and ambient relative humidity (RH), have large influences on LR. It is found that the
56 ratio of σ_{ext} and β_{sca} grows linearly but slowly as RH increases when RH is lower than 80% (Salemink
57 et al., 1984) . Different types of aerosols may correspond to different behaviors of LR under different
58 conditions (Ackermann, 1998). Further research found that LR is likely to change significantly due to
59 the substantial variation of RH in the mixed layer (Ferrare et al., 1998). Small errors from the initial

60 conditions may lead to large bias of retrieved σ_{ext} profiles (Sušnik et al., 2014). It is likely that using a
61 constant LR profile instead of variable LR profile to retrieve elastic-backscatter lidar data may result in
62 significant bias of retrieved σ_{ext} profiles. The sounding profiles show that RH is highly variable and
63 frequently beyond 80% in the mixed layer in the NCP (Kuang et al., 2016) which is one of the most
64 polluted areas around the world (Ma et al., 2011; Xu et al., 2011). According to this, it is interesting to
65 know how much σ_{ext} profiles retrieved from elastic-backscatter lidar signals will be deviated if
66 constant column-related LR profile is used in the NCP. Few works have been done to assess the bias of
67 using a constant LR profile.

68 In this research, influences of aerosol hygroscopic growth on LR by using Mie theory (Bohren and
69 Huffman, 2007a) and κ -Köhler theory (Petters and Kreidenweis, 2007) are studied and a further
70 discussion about impacts of RH profiles on LR profiles are carried out. Several simulations are
71 performed to study how much the σ_{ext} profiles will be affected if constant column-related LR profiles
72 are used. Sensitivity tests are also carried out to investigate the variability of the bias caused by using
73 constant column-related LR profiles under different pollution levels. Based on conducted analysis, a
74 feasible method is proposed to decrease the bias of σ_{ext} profiles retrieved from the elastic-backscatter
75 lidar signals. Finally, real-time field measurements of micro-pulsed lidar (MPL) signals are used to
76 validate this method.

77 **2. Data**

78 **2.1 Datasets of aerosol properties**

79 During the first period of Haze in China (HaChi) campaign
80 (http://www.atmos-chem-phys.net/special_issue226.html), the physical and chemical properties of
81 aerosol particles were measured at the Wuqing meteorological station. Wuqing site is located between
82 two megacities (Beijing and Tianjin) of NCP, and can represent the pollution conditions of the NCP
83 (Xu et al., 2011). This study uses the measured datasets of PNSD, black carbon (BC) (Ma et al., 2012)
84 and aerosol hygroscopicity (Chen et al., 2014; Liu et al., 2014) during the field campaign. Details
85 about this field campaign and instruments used can be found in the references.

86 **2.2 RH profiles**

87 The intensive GTS1 observation (Bian et al., 2011) at the meteorological bureau of Beijing (39°48'
88 N, 116°28' E) were carried out from July to September in 2008. With a resolution of 10m in the vertical
89 direction, the radiosonde data includes profiles of temperature, pressure and RH. During the intensive

90 observation period, balloon soundings were performed four times a day.

91 Water vapor mixing ratio is almost constant in the mixed layer due to extensive turbulent mixing
92 existing and decreases rapidly above the mixed layer. RH profiles that exhibit well-mixed vertical
93 structures are picked out and studied. With this, the maximum RH in the vertical direction can be used
94 as a good representation of RH profiles. RH profiles are classified into four typical groups based on the
95 maximum RH ranges: 60%-70%, 70%-80%, 80%-90% and 90%-95% (Kuang et al., 2016). These four
96 kinds of typical well-mixed RH profiles are labeled as P60-70, P70-80, P80-90 and P90-95
97 respectively.

98 **2.3 MPL signals**

99 A single wavelength polarization diversity elastic lidar system is installed on the roof of the
100 physics building in Peking University. This instrument is a MPL manufactured by Sigma Space, using
101 a Nd: YVO4 532nm pulsed DC10H-532SS laser source, with a pulse duration of 10.3ns, energy of
102 6-8uJ and a repetition of 2500Hz. It collects elastically backscattered signals from the atmosphere by
103 separately detecting its parallel and cross polarization components with respect to the polarization of
104 laser. Concurrently measured AOD data comes from the AERONET BEIJING_PKU station, which is
105 located at the same place as the Lidar.

106 **3. Methodology**

107 **3.1 Influences of aerosol hygroscopic growth on LR**

108 In this research, the Mie model (Bohren and Huffman, 2007a) is used to study the influence of RH
109 on LR. The results of Mie model contains the information of the σ_{ext} and β_{sca} , which can be used to
110 derived the LR directly. When running the Mie model, aerosol PNSD, aerosol complex refractive
111 index, RH, black carbon mixing state and black carbon concentration are essential.

112 Mixing states of BC come from the measurement during the Hachi Campaign. In previous work,
113 BC mixing states during the Hachi campaign were presented as both core-shell mixed and externally
114 mixed (Ma et al., 2012). Ma et al. (2012) provides the ratio of BC mass concentration under externally
115 mixed state to total BC mass concentration as follows:

$$116 \quad r_{\text{ext}_{BC}} = \frac{M_{\text{ext}_{BC}}}{M_{BC}} \quad (1).$$

117 $M_{\text{ext}_{BC}}$ is the mass concentration that is externally mixed and M_{BC} is the total mass concentration of
118 BC. The mean value of $r_{\text{ext}_{BC}}$ is used as a representation of the mixing state in this study. The

119 size-resolved distribution of BC mass concentration is the same as that used by Ma et al (2012a).

120 As for the aerosol hygroscopicity, the size-resolved hygroscopicity parameter κ (Petters and
121 Kreidenweis, 2007) introduced in (Chen et al., 2012) is used to account for aerosol hygroscopic growth.
122 The size-resolved hygroscopicity parameter κ is derived from the aerosol hygroscopic growth factor
123 measured by High Humidity Tandem Differential Mobility Analyzer. Size-resolved κ with high time
124 resolution is derived by using the HaChi Campaign measurement data (Chen et al., 2012; Liu et al.,
125 2011). The mean value of size-resolved κ is used to account for the mean hygroscopicity of aerosols in
126 this study.

127 The refractive index (\tilde{m}) considering the water content in the particle, is derived as a volume
128 mixture between the dry aerosol and water (Wex et al., 2002):

$$129 \quad \tilde{m} = f_{V,dry} \tilde{m}_{aero,dry} + (1 - f_{V,dry}) \tilde{m}_{water} \quad (2).$$

130 $f_{v,dry}$ is the ratio of the dry aerosol volume to total aerosol volume at given RH condition; $\tilde{m}_{aero,dry}$ is
131 the refractive index of dry ambient aerosols and \tilde{m}_{water} is the refractive index of water content
132 absorbed by aerosols.

133 For each measured aerosol PNSD under dry condition, the corresponding aerosol PNSD at a given
134 RH can be calculated. Aerosol refractive index can be determined, too. With this information, LR can
135 be obtained. Different LR values under different RH conditions are available.

136 The LR enhancement factor is introduced to describe the influence of aerosol hygroscopic growth
137 on LR at different RH. It is defined as the ratio of LR at a given RH to LR at the condition of
138 $RH < 40\%$.

139 **3.2 LR profiles and σ_{ext} profiles**

140 Assumptions about aerosol properties in the vertical direction are made to calculate LR profiles
141 and σ_{ext} profiles.

142 Liu et al. (2009) studied vertical profiles of aerosol total number concentration (Na) with aircraft
143 measurements. Vertical distributions of Na are parameterized according to the vertical distribution
144 properties of Na. Results showed that Na is relatively constant in the mixed layer. A transition layer
145 where Na linearly decreases exists in the parameterized scheme. Na also exponentially decreases
146 above the transition layer. The same parameterized scheme proposed by Liu et al. (2009) is adopted by
147 this study. Both the study of Liu et al. (2009) and Ferrero et al. (2010) manifests that the dry aerosol
148 PNSD in the mixed layer varies little. The shape of dry aerosol PNSD is assumed constant along with

149 the height, which means that aerosol PNSD at different heights divided by Na give the same
150 normalized PNSD.

151 As for the BC vertical distribution, Ferrero et al. (2011) and Ran et al. (2016) demonstrate that BC
152 mass concentration in the mixed layer remains relatively constant and decreases sharply above the
153 mixed layer. According to this, parameterization scheme of BC vertical distributions is assumed the
154 same as that of the aerosol. The shape of the size-resolved BC mass concentration distribution is also
155 assumed the same as that at the surface.

156 LR profiles and σ_{ext} profiles can be calculated by Mie theory under these assumptions. Details of
157 computing σ_{ext} profiles can be found at Kuang et al. (2015).

158 **3.3 Simulated elastic-backscatter lidar signals**

159 The intensity of signals received by elastic-backscatter lidar depends on optical properties of
160 objects and the distance between scattering objects and receiving system. It can be typically described
161 by the following formula:

$$162 \quad P(R) = C \times P_0 \times \frac{\beta(R)}{R^2} \times e^{\int_0^R -2 \times \sigma(r) \times dr} \quad (3).$$

163 In equation (3), P_0 is the intensity of the laser pulse. R is the spatial distance between scattering
164 objects and the receiving system. C is a correction factor determined by the status of
165 elastic-backscatter lidar machine itself. $\beta(R)$ refers to the sum of aerosol backscattering coefficient
166 (β_{sca}) and air molecule backscattering coefficient ($\beta_{\text{sca,mole}}$) at distance R . $\sigma(R)$ denotes the sum of σ_{ext}
167 and air molecule's extinction coefficient ($\sigma_{\text{ext,mole}}$). $\beta_{\text{sca,mole}}$ and $\sigma_{\text{ext,mole}}$ can be calculated by using
168 Rayleigh scattering theory when the temperature and pressure are available.

169 In this study, we can theoretically get the intensities of elastic-backscatter lidar signals from each
170 given σ_{ext} and β_{sca} profiles with the assumption that C is equal to one. Retrieving elastic-backscatter
171 lidar signals can result in exactly the same σ_{ext} profile as the original one when the profile of LR is
172 available. However, a constant column-related LR profile is used to retrieve elastic-backscatter lidar
173 signals and the retrieved σ_{ext} profile would deviate from the given σ_{ext} profile when there is insufficient
174 information about the LR profile.

175 **3.4 Retrieving σ_{ext} profiles from elastic-backscatter lidar signals**

176 **3.4.1 Retrieving σ_{ext} profiles by using constant column-related LR profile method**

177 Additional information is needed to get the mathematical results of formula (3) because there are

178 two unknown parameters (β_{sca} and σ_{ext}). The commonly used method of solving this formula is to
179 assume a constant value of column-related LR and then the profiles of σ_{ext} and β_{ext} can be retrieved
180 (Fernald, 1984; Klett, 1985). Different values of column-related LR can lead to different σ_{ext} profiles
181 and different AOD. A constant column-related LR can be constrained if sun photometer are
182 concurrently measuring the AOD (He et al., 2006; Pietruczuk and Podgorski, 2009). Thus, σ_{ext} profile
183 can be retrieved by using the column-related constant LR profile.

184 **3.4.2 Retrieving σ_{ext} profiles accounting for aerosol hygroscopic growth**

185 A new method of retrieving σ_{ext} profiles from elastic-backscatter lidar signals is proposed, in
186 which the variation of LR with RH can be taken into consideration. A schematic diagram of this
187 method is shown in Fig.1. A parameterized LR profile is used to retrieve σ_{ext} profiles instead of an
188 AOD-constrained constant LR profile. Firstly, the LR enhancement factor are statistically studied and
189 parameterized under different polluted conditions. LR profile can be calculated using RH profile and
190 LR value at dry state. σ_{ext} profile can be retrieved with combination of LR profile and formula (3). Dry
191 state LR value can be constrained by comparing the integrated AOD value of retrieved σ_{ext} profile and
192 concurrently measured AOD value. LR profile is determined and σ_{ext} profile can be retrieved with the
193 constrained dry state LR.

194 **4. Results and Discussion**

195 **4.1 LR properties**

196 **4.1.1 Variation of LR with RH**

197 During the field campaign of Hachi, there were a total of 3540 different aerosol PNSDs. LR is
198 calculated by using different aerosol PNSD and RH values between 30% and 95%.

199 Relationships between dry state LR and concurrently measured σ_{ext} (sum of the aerosol scattering
200 and absorption) are shown in Fig. 2(a). It shows that LR can vary across a wide range from 30 sr to 90
201 sr, which is consistent with the literature values of continent aerosols (Ansmann et al., 2001;
202 Pappalardo et al., 2004a). This also indicates that calculating the LR by using Mie theory is feasible.
203 Fig. 2(b) gives the probability distribution function of the LR. Most of the LR lies in the range between
204 45~65 sr.

205 In order to have a better understanding of the relationship between aerosol PNSD and LR,
206 lognormal distributions of aerosol PNSD are used to fit the PNSD of aerosol particles. Firstly, the sum
207 of four different lognormal modes, which are known as Nucleation mode, Aitken mode, Accumulation

208 mode and Coarse mode, are used to fit the distribution of aerosol PNSD (Chen et al., 2012; Hussein et
 209 al., 2005; Mattis et al., 2002). Details of this method can be found in Chen et al. (2012). LR values at
 210 different modes are accordingly calculated by using Mie scattering theory. For each aerosol PNSD, we
 211 can get one LR value by using the measured aerosol PNSD, and another four LR values by using four
 212 derived lognormal mode aerosols respectively. Finally, LR based on the total PNSD is regressed on
 213 derived LR from the four lognormal modes.

214 Table 1 gives the statistical results of the LR range and the correlation coefficients. Results show
 215 that Accumulation mode aerosol contributes the most to the LR at 61% with a mean value of 56.04 sr.
 216 The LR from Aitken mode comes second, with a contribution of 19% and a mean value of 42.15 sr.
 217 The Nucleation mode aerosol gives a mean LR value of 9.72 sr, which is almost the same as the LR of
 218 air molecules ($\frac{8\pi}{3}$ sr) and contributes only 3% to the total LR. The Coarse mode gets 5% partition of
 219 total LR with mean value of 97 sr. It can be concluded that the Accumulation mode of the aerosols
 220 should be taken into account first when deriving PNSD information from the LR signals.

221 Relationships between the LR enhancement factor and RH are given in Fig. 2(c). The LR
 222 enhancement factor has a mean value lower than 1.2 when the RH is lower than 70%. LR increases
 223 linearly with RH when RH is lower than 80%, which is consistent with the literal results (Salemink et
 224 al., 1984). However, LR can be enhanced by a factor of 2.2 when the RH reaches 92% with mean
 225 hygroscopicity of aerosol. There tends to be more forward scattering and less backscattering at 180°
 226 when aerosol particles grow bigger according to Mie theory (Bohren and Huffman, 2007b). With this,
 227 LR value is larger when the particles grow larger.

228 Mean values of LR enhancement factor are parameterized as below:

$$229 \quad RH_0 = RH - 40 \quad (4)$$

$$230 \quad LR = LR_{dry} \times (0.92 + 2.5 \times 10^{-2}RH_0 - 1.3 \times 10^{-4}RH_0^2 + 2.2 \times 10^{-5}RH_0^3) \quad (5).$$

231 This parameterization equation can be used as a representation of the mean effect of continental
 232 aerosol hygroscopicity on LR.

233 4.1.2 LR ratio profiles

234 Fig.3 shows four different types of RH profiles and LR profiles. Fig. 3(a) shows RH profiles of
 235 P60-70, P70-80, P80-90 and P90-95 respectively. In Fig. 3(a), RH values increase with height in the
 236 mixed layer and decrease with height above the mixed layer. This is a result of temperature and water

237 content distributions in the vertical direction. In the mixed layer, water vapor is well mixed within the
238 mixed layer and decreases sharply above the mixed layer. P60-70 can represent the relatively dry
239 conditions on a summer afternoon. Statistical results show that P80-90 is most likely to be observed in
240 the environment. P90-95 is a very moist environment condition and its frequency of being observed is
241 second to that of the P80-90 type.

242 Profiles of LR corresponding to RH profiles of the left column are shown in Fig. 3(b). For each
243 type of LR profile, LR increases with height in the mixed layer due to the increase of RH. At the
244 ground, the mean values of LR for each RH profiles are 38.19, 38.28, 39.53 and 40.33 sr, with a
245 standard deviation of 6.20, 6.22, 6.42 and 6.45 respectively. LR changes little from 38 sr at the ground
246 to 42 sr at the top of the mixed layer when the ambient RH is low for the RH profile of P60-70.
247 However, LR grows with a mean value from 40 sr to 60 sr with a relative difference of 50% when the
248 RH is high for the RH profile of P90-95. With such high variation of LR with RH, the retrieved σ_{ext}
249 profiles might be greatly deviated when using a constant LR profile instead of a variable one.

250 The black dotted line in Fig. 3(b) is one of the constant column-related LR profiles that are used as
251 an input of retrieving σ_{ext} profiles related to the RH profile P70-80. The constant LR has a higher value
252 at the ground and a lower value at the top of the mixed layer when compared with the calculated
253 variable LR profiles.

254 During the Hachi Campaign, LR values that are calculated by using Mie theory can change from
255 30 to 55 sr within 12 hours at the ground (about 87% of initial value). With high variation of LR over
256 time, the LR profile should be updated in time to get an accurately retrieved σ_{ext} profile. Using only
257 one measurement of LR profile to retrieve the σ_{ext} profiles may lead to great bias of retrieved results
258 (Rosati et al., 2016).

259 **4.2 Bias of retrieved σ_{ext} profiles**

260 **4.2.1 Retrieved σ_{ext} profiles vs. original σ_{ext} profiles**

261 Fig. 4 provides an example of the retrieved σ_{ext} profile by using the variable LR profile method
262 and that by using the constant LR profile method from simulated lidar signals. These two kinds of
263 profiles can also be described as a given parameterized σ_{ext} profile and a retrieved σ_{ext} profile from
264 constant LR profile. In Fig. 4(a), the retrieved σ_{ext} profile by using a variable LR profile method is
265 demonstrated by solid line. Dotted line shows the retrieved σ_{ext} profile by using a constant column
266 related LR method. Fig. 4(b) shows the relative bias of the two retrieved σ_{ext} profiles at each height.

267 Fig. 4(c) and (d) are almost the same as Fig. 4(a) and (b) respectively, except that the results of Fig. 4(a)
268 and (b) come from the RH profile of P70-80 while those of Fig. 4(c) and (d) come from the RH profile
269 of P90-95.

270 It is shown in Fig. 4(a) that the retrieved σ_{ext} by using a variable LR profile method increases with
271 height at a rate of $92.25 \text{ (Mm}^{-1}\text{km}^{-1}\text{)}$ in the mixed layer, which is consistent with the aerosol loading
272 and RH distribution. However, the retrieved σ_{ext} profile by using a constant LR profile method behaves
273 differently and decreases at a rate of $-152.87 \text{ (Mm}^{-1}\text{km}^{-1}\text{)}$. The structure of σ_{ext} profiles is different by
274 using two different methods. Moreover, the retrieved σ_{ext} from RH profile of P90-95 at the top of the
275 mixed layer is significantly deviated with a relative bias of 40%.

276 Both Fig. 4(a) and (c) show that the retrieved σ_{ext} is overestimated at ground and underestimated at
277 the top of the mixed layer. From Fig 3(b), it can be concluded that the AOD-constrained constant LR is
278 larger than the calculated true LR at the ground and smaller at the top of the mixed layer. According to
279 formula (3), signals of the elastic-backscatter lidar received at any height are proportional to the
280 backscattering capability of the aerosols. When LR is larger, a larger fraction of the signals transfer
281 forward and less is scattered back. In order to receive the same amount of signal, the backscattering
282 coefficient should be larger and this can lead to the result of a larger σ_{ext} at that layer. Thus, the σ_{ext}
283 tends to be biased higher than the given parameterized σ_{ext} when the LR is larger, and vice versa.
284 Overall, the profiles retrieved by using an AOD-constrained LR can lead to a positive bias at the
285 ground and a negative bias at the top of mixed layer.

286 **4.2.2 Sensitivity Study**

287 Simulations are conducted to study the characteristics of the retrieved σ_{ext} profile bias between
288 using the constant column-related LR profile and variable LR profile. Different kinds of aerosol PNSD,
289 AOD, aerosol hygroscopicity and RH profiles are used. Aerosol PNSD data comes from the Hachi
290 Campaign field measurement. The sensitivity of the bias in aerosol hygroscopicity is evaluated by
291 changing the size-resolved κ value. Aerosols are defined to have high hygroscopicity when the aerosol
292 size-resolved κ value is one standard deviation above the mean of the size-resolved κ value. They are
293 defined as low hygroscopicity if the size-resolved κ value is one standard deviation below mean of the
294 size-resolved κ value. Four different kinds of RH profiles are also used in this sensitivity study. As
295 discussed in section 3.2.1, a negative bias at the top of the mixed layer is accompanied by a positive
296 bias at the ground and the largest bias happens at the top of the mixed layer. It is sufficient to focus on

297 the relative bias at the top of the mixed layer.

298 Statistical characteristics of the relative bias at the top of the mixed layer are shown in Fig. 5.
299 Different panels represent the results of different aerosol hygroscopicity. The left column shows the
300 results of low aerosol hygroscopicity. Middle panel shows results from mean aerosol hygroscopicity.
301 High aerosol hygroscopicity of particles results in the properties shown in the right panel. For each
302 panel, relationships between relative bias and AOD are shown. Different colors in each panel show the
303 results of different RH profiles. Filled colors represent the ranges of the relative bias at one standard
304 deviation of using different PNSD.

305 Every panel show that relative bias clearly increases with the enhancement of RH in the
306 surroundings. The relative bias has a mean value of less than 10% for RH profile of P60-70. LR has
307 little variation when the surrounding RH is low and the bias has a low value. For RH profiles of
308 P70-80 and P80-90, the relative bias increases with RH and increases strongly up to 25% when the
309 surrounding relative humidity is high. These behaviors of relative difference under difference RH
310 conditions are consistent with the change of LR with RH.

311 Filled color ranges of relative bias at given AOD and RH profile result from the variation of
312 aerosol PNSD. The LR enhancement factor can have different behavior with different aerosol PNSD
313 according to Mie scattering theory. Changing the aerosol PNSD leads to a wider range of bias when
314 the RH is higher. Fig. 5 also shows that different PNSD can change the relative bias by a mean value
315 of 10% for different polluted conditions.

316 Relative bias increases with AOD value when the AOD is low, while it remains constant when the
317 AOD is high. When AOD is low, the amount of scattered light by air molecules occupies a large
318 fraction. Air molecules have a constant LR of $\frac{8}{3}\pi$ sr according the Rayleigh scattering theory. The
319 relative bias of retrieved σ_{ext} profile is relatively small when the AOD is low. When the AOD has a
320 larger value, backscattered signals mainly depend on aerosol backscattering and the signals
321 backscattered by air molecules are negligible. Relative bias mainly reflects the impacts of aerosol
322 hygroscopicity. The mean relative bias increases from 26% to 32% at high RH conditions with the
323 increase of aerosol hygroscopicity. Aerosol hygroscopicity should be taken into account under high
324 RH conditions.

325 To sum up, RH is one of the most important factors that influence the accuracy of retrieving the

326 elastic-backscatter lidar data. Different PNSD can also lead to a large variation of relative difference.
327 The relative difference increases with the AOD when the AOD is low, but increases little when the
328 AOD is high. Under the conditions of both high values of RH and AOD, the relative bias of retrieved
329 data reaches a maximum due to the influence of aerosol hygroscopic growth.

330 **4.3 Evaluation of LR enhancement factor parameterization**

331 Simulations were carried out to test the efficiency of LR the enhancement factor parameterization
332 scheme. All of the simulations in section 4.2 were conducted again by using the method of 3.4.2. The
333 relative bias between the parameterized σ_{ext} profile and the retrieved σ_{ext} profile by using the
334 parameterized LR enhancement factor scheme are studied and summarized in Table 2. The values
335 listed in Table 2 are the mean results under different PNSD conditions. From Table 2, we can see that
336 all of the relative bias is within the range of 13%. This indicates that the new algorithm using the mean
337 LR enhancement factor parameterization scheme is robust and can decrease the bias of the retrieved
338 elastic-backscatter lidar data significantly.

339 **4.4 Retrieving the real-time measurement elastic-backscatter lidar signals**

340 MPL data and AERONET data are employed to validate the algorithm of retrieving the
341 elastic-backscatter lidar data on the day of 5 July 2016. After quality control of data processing,
342 elastic-backscatter lidar data is retrieved by using both a constant LR profile method and a
343 parameterized variable LR profile method. Fig. 6 shows the retrieved σ_{ext} profiles using two methods
344 of local time 13:00 (a) and 14:30 (b).

345 Fig. 6(a) is a typical case of the retrieved σ_{ext} profiles under high values of both RH and AOD
346 conditions. The retrieved σ_{ext} profiles by using the constant LR profile method and variable LR profile
347 method show almost the same properties as the simulations. The relative bias reaches a value of 39.3%
348 at an altitude of 1.57 km. These differences of retrieved σ_{ext} profiles may lead to a significant bias of
349 estimating the mixed layer height and have significant impact on radiative energy distribution in the
350 vertical direction. Fig. 6(b) shows the retrieved σ_{ext} profiles of different structures from the same
351 elastic-backscatter lidar data. The retrieved σ_{ext} by using variable LR profile method increases with
352 height within the mixed layer. However, the retrieved σ_{ext} by using constant LR profile decreases
353 slightly with height within the mixed layer.

354 **5 Conclusions**

355 The influence of aerosol hygroscopic growth on LR is evaluated by using Mie scattering theory.

356 Datasets used as input to Mie theory model come from the Hachi Campaign field measurements.
357 Results show that LR in the NCP mainly ranges from 30 to 90 sr, which is consistent with literature
358 values of continental aerosols. LR could be enhanced significantly under high RH conditions, with a
359 mean factor of 2.2 at 92% RH.

360 RH in the mixed layer in the NCP is frequently observed to be higher than 90%. Under these
361 conditions, large variation of LR in the vertical direction exists. This leads to significant bias of
362 retrieved σ_{ext} profile due to a constant LR profile currently used to retrieve the elastic-backscatter lidar
363 signals. The relative bias of the retrieved σ_{ext} profiles between the constant LR profile method and the
364 variable LR profile method can reach up to 40% under high RH conditions and the retrieved σ_{ext}
365 profile structure can be different under low RH conditions.

366 Sensitivity studies are carried out to test the bias of retrieved σ_{ext} profiles. The bias increases
367 linearly with RH at low RH but increases strongly at high RH. PNSD can lead to 10% standard
368 deviation of the bias. Maximum bias happens under the conditions of both high AOD and RH that
369 frequently happen in the NCP. The influence of aerosol hygroscopic growth on LR should be taken
370 into consideration when retrieving the elastic-backscatter lidar data in the NCP.

371 A new algorithm accounting for the aerosol hygroscopic growth is proposed to retrieve the
372 elastic-backscatter lidar data. A scheme of LR enhancement factor parameterization is introduced in
373 this algorithm. The bias of retrieved σ_{ext} profiles by using this algorithm can be constrained within
374 13%. Real-time measurement of MPL data is employed to validate the algorithm and the results show
375 good consistency with the simulations.

376 This research will advance our understanding of the influence of aerosol hygroscopic growth on
377 LR and help to improve the retrieval of σ_{ext} profile from elastic-backscatter lidar signals.

378

379 **Acknowledgments**

380 This work is supported by the National Natural Science Foundation of China (41590872,
381 41375134).

382

383

384 **References**

385 Ackermann, J. (1998) The Extinction-to-Backscatter Ratio of Tropospheric Aerosol: A Numerical Study. *Journal of*
386 *Atmospheric and Oceanic Technology* 15, 1043-1050.

387 Anderson, T.L., Anderson, T.L. (2003) Variability of aerosol optical properties derived from in situ aircraft measurements
388 during ACE-Asia. *Journal of Geophysical Research* 108, ACE-15-11-ACE 15-19.

389 Andreae, M.O., Crutzen, P.J. (1997) Atmospheric Aerosols: Biogeochemical Sources and Role in Atmospheric Chemistry.
390 *Science* 276, 1052-1058.

391 Ansmann, A., Wagner, F., Althausen, D., Müller, D., Herber, A., Wandinger, U. (2001) European pollution outbreaks during
392 ACE 2: Lofted aerosol plumes observed with Raman lidar at the Portuguese coast. *Journal of Geophysical Research*
393 *Atmospheres* 106, 20725–20733.

394 Ansmann, A., Wagner, F., Müller, D., Althausen, D., Herber, A., von Hoyningen-Huene, W., Wandinger, U. (2002) European
395 pollution outbreaks during ACE 2: Optical particle properties inferred from multiwavelength lidar and star-Sun photometry.
396 *Journal of Geophysical Research: Atmospheres* 107, AAC 8-1-AAC 8-14.

397 Bian, J., Chen, H., Ouml, mel, H., Duan, Y. (2011) Intercomparison of humidity and temperature sensors: GTS1, Vaisala RS80,
398 and CFH. *Advances in atmospheric sciences* 28, 139-146.

399 Bohren, C.F., Huffman, D.R., (2007a) Absorption and Scattering by an Arbitrary Particle, *Absorption and Scattering of Light*
400 *by Small Particles*. Wiley-VCH Verlag GmbH, pp. 57-81.

401 Bohren, C.F., Huffman, D.R., (2007b) Angular Dependence of Scattering, *Absorption and Scattering of Light by Small*
402 *Particles*. Wiley-VCH Verlag GmbH, pp. 381-428.

403 Chaikovsky, A., Dubovik, O., Holben, B., Bril, A., Goloub, P., Tanre, D., Pappalardo, G., Wandinger, U., Chaikovskaya, L.,
404 Denisov, S., Grudo, J., Lopatin, A., Karol, Y., Lapyonok, T., Amiridis, V., Ansmann, A., Apituley, A., Allados-Arboledas, L.,
405 Biniatoglou, I., Boselli, A., D'Amico, G., Freudenthaler, V., Giles, D., Jose Granados-Munoz, M., Kokkalis, P., Nicolae, D.,
406 Oshchepkov, S., Papayannis, A., Perrone, M.R., Pietruczuk, A., Rocadenbosch, F., Sicard, M., Slutsker, I., Talianu, C., De
407 Tomasi, F., Tsekeri, A., Wagner, J., Wang, X. (2016) Lidar-Radiometer Inversion Code (LIRIC) for the retrieval of vertical
408 aerosol properties from combined lidar/radiometer data: development and distribution in EARLINET. *Atmospheric*
409 *Measurement Techniques* 9, 1181-1205.

410 Chen, J., Zhao, C.S., Ma, N., Liu, P.F., Göbel, T., Hallbauer, E., Deng, Z.Z., Ran, L., Xu, W.Y., Liang, Z., Liu, H.J., Yan, P., Zhou,
411 X.J., Wiedensohler, A. (2012) A parameterization of low visibilities for hazy days in the North China Plain. *Atmos. Chem.*
412 *Phys.* 12, 4935-4950.

413 Chen, J., Zhao, C.S., Ma, N., Yan, P. (2014) Aerosol hygroscopicity parameter derived from the light scattering enhancement
414 factor measurements in the North China Plain. *Atmos. Chem. Phys.* 14, 8105-8118.

415 Fernald, F.G. (1984) Analysis of atmospheric lidar observations: some comments. *Applied Optics* 23, 652-653.

416 Fernald, F.G., Herman, B.M., Reagan, J.A. (1972) Determination of Aerosol Height Distributions by Lidar. *Journal of Applied*
417 *Meteorology* 11, 482-489.

418 Ferrare, R.A., Melfi, S.H., Whiteman, D.N., Evans, K.D., Poellot, M., Kaufman, Y.J. (1998) Raman lidar measurements of
419 aerosol extinction and backscattering: 2. Derivation of aerosol real refractive index, single-scattering albedo, and
420 humidification factor using Raman lidar and aircraft size distribution measurements. *Journal of Geophysical Research:*
421 *Atmospheres* 103, 19673-19689.

422 Ferrero, L., Mocnik, G., Ferrini, B.S., Perrone, M.G., Sangiorgi, G., Bolzacchini, E. (2011) Vertical profiles of aerosol
423 absorption coefficient from micro-Aethalometer data and Mie calculation over Milan. *Science of the Total Environment*
424 409, 2824-2837.

425 Ferrero, L., Perrone, M.G., Petraccone, S., Sangiorgi, G., Ferrini, B.S., Lo Porto, C., Lazzati, Z., Cocchi, D., Bruno, F., Greco, F.,
426 Riccio, A., Bolzacchini, E. (2010) Vertically-resolved particle size distribution within and above the mixing layer over the
427 Milan metropolitan area. *Atmospheric Chemistry and Physics* 10, 3915-3932.

428 Gasteiger, J., Groß, S., Sauer, D., Haorig, M., Ansmann, A., Weinzierl, B. (2017) Particle settling and vertical mixing in the

429 Saharan Air Layer as seen from an integrated model, lidar, and in situ perspective. *Atmospheric Chemistry and Physics* 17,
430 297-311.

431 He, Q.S., Li, C.C., Mao, J.T., Lau, A.K.H., Li, P.R. (2006) A study on the aerosol extinction-to-backscatter ratio with
432 combination of micro-pulse LIDAR and MODIS over Hong Kong. *Atmospheric Chemistry and Physics* 6, 3243-3256.

433 Hussein, T., Maso, M.D., Petäjä, T., Koponen, I.K., Paatero, P., Aalto, P.P., Hämeri, K., Kulmala, M. (2005) Evaluation of an
434 automatic algorithm for fitting the particle number size distributions. *Boreal Environment Research* 10, 337-355.

435 Klett, J.D. (1981) Stable analytical inversion solution for processing lidar returns. *Applied Optics* 20, 211-220.

436 Klett, J.D. (1985) Lidar inversion with variable backscatter/extinction ratios. *Applied Optics* 24, 1638-1643.

437 Kuang, Y., Zhao, C.S., Tao, J.C., Bian, Y.X., Ma, N. (2016) Impact of aerosol hygroscopic growth on the direct aerosol
438 radiative effect in summer on North China Plain. *Atmospheric Environment* 147, 224-233.

439 Kuang, Y., Zhao, C.S., Tao, J.C., Ma, N. (2015) Diurnal variations of aerosol optical properties in the North China Plain and
440 their influences on the estimates of direct aerosol radiative effect. *Atmos. Chem. Phys.* 15, 5761-5772.

441 Liu, H.J., Zhao, C.S., Nekat, B., Ma, N., Wiedensohler, A., van Pinxteren, D., Spindler, G., Müller, K., Herrmann, H. (2014)
442 Aerosol hygroscopicity derived from size-segregated chemical composition and its parameterization in the North China
443 Plain. *Atmospheric Chemistry and Physics* 14, 2525-2539.

444 Liu, P., Zhao, C., Zhang, Q., Deng, Z., Huang, M., Xincheng, M.A., Tie, X. (2009) Aircraft study of aerosol vertical
445 distributions over Beijing and their optical properties. *Tellus Series B-chemical & Physical Meteorology* 61, 756-767.

446 Liu, P.F., Zhao, C.S., Göbel, T., Hallbauer, E., Nowak, A., Ran, L., Xu, W.Y., Deng, Z.Z., Ma, N., Mildenerger, K., Henning, S.,
447 Stratmann, F., Wiedensohler, A. (2011) Hygroscopic properties of aerosol particles at high relative humidity and their
448 diurnal variations in the North China Plain. *Atmos. Chem. Phys.* 11, 3479-3494.

449 Ma, N., Zhao, C.S., Müller, T., Cheng, Y.F., Liu, P.F., Deng, Z.Z., Xu, W.Y., Ran, L., Nekat, B., van Pinxteren, D., Gnauk, T., Müller,
450 K., Herrmann, H., Yan, P., Zhou, X.J., Wiedensohler, A. (2012) A new method to determine the mixing state of light
451 absorbing carbonaceous using the measured aerosol optical properties and number size distributions. *Atmos. Chem. Phys.*
452 12, 2381-2397.

453 Ma, N., Zhao, C.S., Nowak, A., Müller, T., Pfeifer, S., Cheng, Y.F., Deng, Z.Z., Liu, P.F., Xu, W.Y., Ran, L., Yan, P., Göbel, T.,
454 Hallbauer, E., Mildenerger, K., Henning, S., Yu, J., Chen, L.L., Zhou, X.J., Stratmann, F., Wiedensohler, A. (2011) Aerosol
455 optical properties in the North China Plain during HaChi campaign: an in-situ optical closure study. *Atmos. Chem. Phys.* 11,
456 5959-5973.

457 Mattis, I., Ansmann, A., Müller, D., Wandinger, U., Althausen, D. (2002) Dual-wavelength Raman lidar observations of the
458 extinction-to-backscatter ratio of Saharan dust. *Geophysical Research Letters* 29, 20-21-20-24.

459 Pappalardo, G., Amodeo, A., Mona, L., Pandolfi, M., Pergola, N., Cuomo, V. (2004a) Raman lidar observations of aerosol
460 emitted during the 2002 Etna eruption. *Geophysical Research Letters* 31, 179-211.

461 Pappalardo, G., Amodeo, A., Pandolfi, M., Wandinger, U., Ansmann, A., Bösenberg, J., Matthias, V., Amiridis, V., De Tomasi,
462 F., Frioud, M., Iarlori, M., Komguem, L., Papayannis, A., Rocadenbosch, F., Wang, X. (2004b) Aerosol lidar intercomparison
463 in the framework of the EARLINET project. 3. Ramanlidar algorithm for aerosol extinction, backscatter, and lidar ratio.
464 *Applied Optics* 43, 5370-5385.

465 Petters, M.D., Kreidenweis, S.M. (2007) A single parameter representation of hygroscopic growth and cloud condensation
466 nucleus activity. *Atmos. Chem. Phys.* 7, 1961-1971.

467 Pietruczuk, A., Podgórski, J., (2009) The lidar ratio derived from sun-photometer measurements at Belsk Geophysical
468 Observatory, *Acta Geophysica*, p. 476.

469 Pietruczuk, A., Podgorski, J. (2009) The lidar ratio derived from sun-photometer measurements at Belsk Geophysical
470 Observatory. *Acta Geophysica* 57, 476-493.

471 Ran, L., Deng, Z., Xu, X., Yan, P., Lin, W., Wang, Y., Tian, P., Wang, P., Pan, W., Lu, D. (2016) Vertical profiles of black carbon
472 measured by a micro-aethalometer in summer in the North China Plain. *Atmospheric Chemistry and Physics* 16,

473 10441-10454.
474 Rosati, B., Herrmann, E., Bucci, S., Fierli, F., Cairo, F., Gysel, M., Tillmann, R., Größ, J., Gobbi, G.P., Di Liberto, L.,
475 Di Donfrancesco, G., Wiedensohler, A., Weingartner, E., Virtanen, A., Mentel, T.F., Baltensperger, U. (2016) Studying the
476 vertical aerosol extinction coefficient by comparing in situ airborne data and elastic backscatter lidar. *Atmospheric*
477 *Chemistry and Physics* 16, 4539-4554.
478 Salemink, H.W.M., Schotanus, P., Bergwerff, J.B. (1984) Quantitative lidar at 532 nm for vertical extinction profiles and the
479 effect of relative humidity. *Applied Physics B* 34, 187-189.
480 She, C.Y., Alvarez, R.J., Caldwell, L.M., Krueger, D.A. (1992) High-spectral-resolution Rayleigh–Mie lidar measurement
481 of aerosol and atmospheric profiles. *Optics Letters* 17, 541-543.
482 Shipley, S.T., Tracy, D.H., Eloranta, E.W., Trauger, J.T., Sroga, J.T., Roesler, F.L., Weinman, J.A. (1983) High spectral resolution
483 lidar to measure optical scattering properties of atmospheric aerosols. 1: Theory and instrumentation. *Applied Optics* 22,
484 3716-3724.
485 Sroga, J.T., Eloranta, E.W., Shipley, S.T., Roesler, F.L., Tryon, P.J. (1983) High spectral resolution lidar to measure optical
486 scattering properties of atmospheric aerosols. 2: Calibration and data analysis. *Applied Optics* 22, 3725-3732.
487 Sušnik, A., Holder, H., Eichinger, W. (2014) A Minimum Variance Method for Lidar Signal Inversion. *Journal of Atmospheric*
488 *and Oceanic Technology* 31, 468-473.
489 Xu, W.Y., Zhao, C.S., Ran, L., Deng, Z.Z., Liu, P.F., Ma, N., Lin, W.L., Xu, X.B., Yan, P., He, X., Yu, J., Liang, W.D., Chen, L.L. (2011)
490 Characteristics of pollutants and their correlation to meteorological conditions at a suburban site in the North China Plain.
491 *Atmos. Chem. Phys.* 11, 4353-4369.
492
493

494 **Table 1** Calculated LR of four lognormal modes PNSD. R^2 is the correlation coefficient of the LR from the lognormal mode PNSD
495 and LR from the total PNSD.

Mode	Diameter (nm)	LR(sr)	R^2
Nuclei mode	19.40	9.72	0.03
Aitken mode	70.11	42.15	0.19
Accumulation mode	239.90	56.04	0.61
Coarse mode	1451	92.93	0.05

496

497

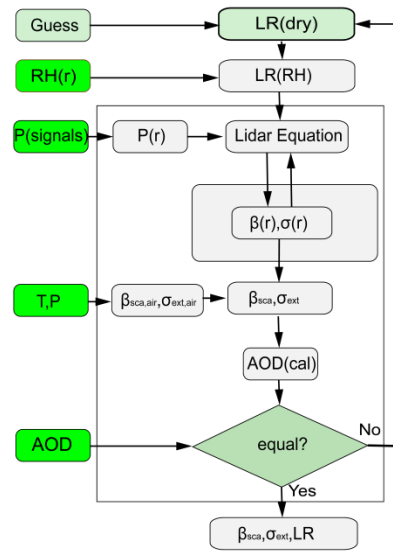
498 **Table 2 Relative difference (%) of the extinction coefficient profiles between using the parameterized LR enhancement factor and**
 499 **the presumed LR under different AOD and RH profile conditions**

		AOD							
		0.2	0.4	0.6	0.8	1.0	1.2	1.4	1.6
RH profile	P60-70	6	9	11	13	8	8	8	9
	P70-80	7	7	9	12	7	6	7	8
	P80-90	8	5	4	11	6	5	5	6
	P90-95	9	6	6	9	13	7	7	9

500

501

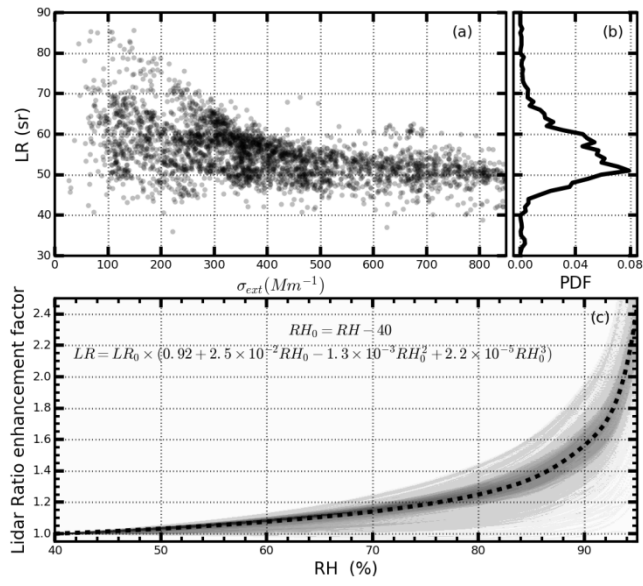
502



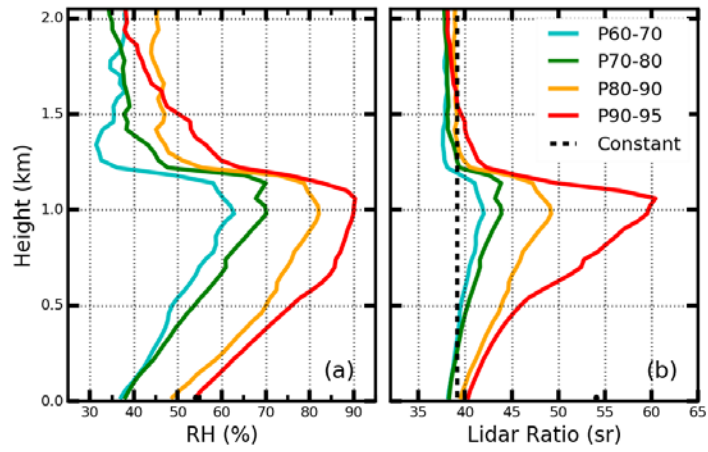
503

504 **Figure 1.** Schematic diagram of retrieving the σ_{ext} profile. The input variables are displayed in green background.

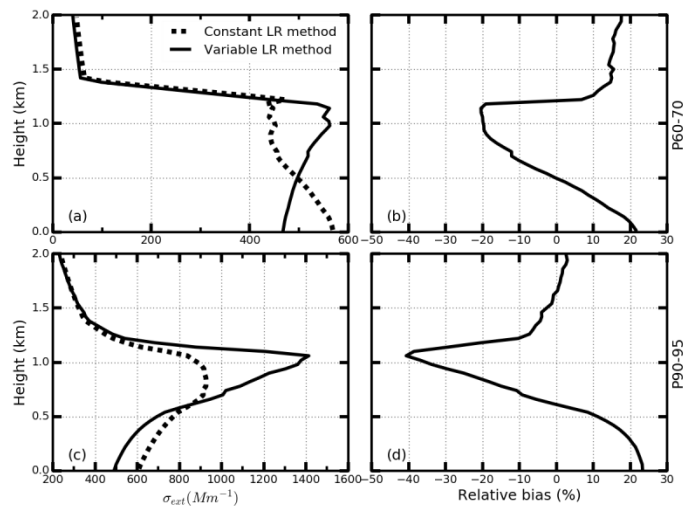
505



506
 507 **Figure 2.** LR distribution and LR enhancement factor during Hachi campaign. (a) LR distribution under different
 508 polluted conditions. (b) Probability distribution of the LR. (c) Enhancement factor of the LR. Dotted line is the mean
 509 fit LR enhancement factor.
 510

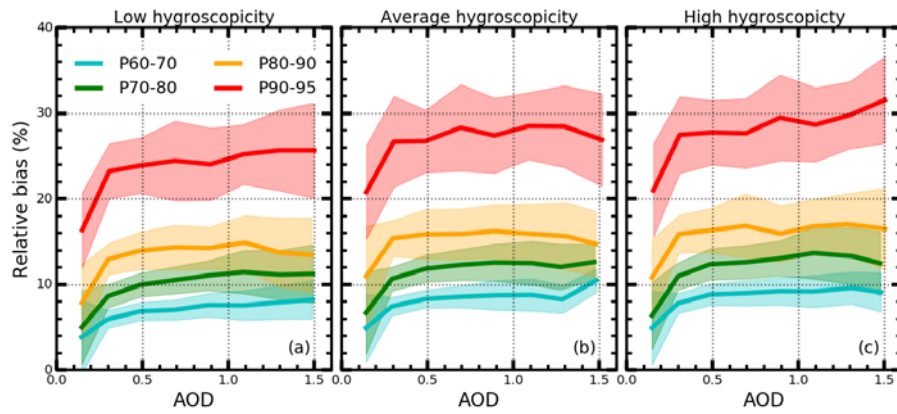


511
 512 **Figure 3.** (a) Four kinds of RH profiles P60-70, P70-80, P80-90, and P90-95; (b) LR profiles from given RH profiles
 513 respectively. Dotted black line is one of the constant LR profile from RH profile of type P70-80 used for retrieving
 514 the MPL signals.
 515

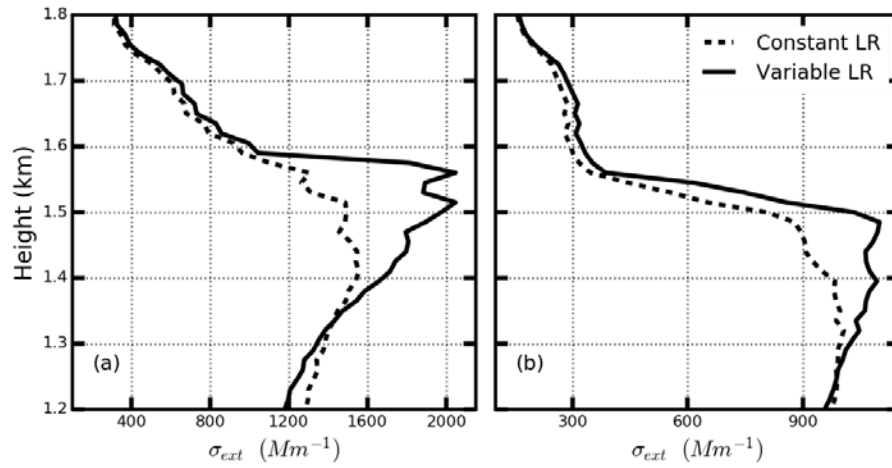


517

518 **Figure 4.** (a) Retrieved σ_{aero} profiles using constant LR profile method (dotted line) and variable LR profile method
 519 (solid line) from simulated lidar signals. (b) The relative bias of the retrieved σ_{aero} profile using two different methods.
 520 (c),(d) are the same as (a), (b) respectively. The LR signals of panel (a) results form P70-80 RH profile, and LR
 521 signals of panel (b) results from P90-95 RH profile



522
 523 **Figure 5.** Relative bias of the retrieved σ_{ext} under different AOD, PNSD, and hygroscopicity and RH profiles
 524 conditions. Different colors represent different RH profile. Panel (a) is derived from the low hygroscopicity. Panel (b)
 525 results from the mean hygroscopicity. Panel (c) is for high hygroscopicity.



526
 527 **Figure 6.** Retrieved σ_{ext} profiles from field measurement MPL signals at (a) 13:00 and (b) 14:30 on July 5, 2016. Dotted
 528 line represents the retrieved σ_{ext} profiles using constant LR profile method. Solid line represents the retrieved σ_{ext} profiles
 529 using variable LR profile method.